Effect of crystal orientations and precipitates on corrosion behavior of Al−Cu−Li single crystals

Feng WEN[1], Ji-qiang CHEN[1,2], Shuang HAN[1], Zi-xiang ZHOU[1],
Shi-biao ZHONG[1], Ying-hui ZHANG[1], Wei-rong LI[2], Ren-guo GUAN[1,3]

1. Faculty of Materials, Metallurgy and Chemistry,
Jiangxi University of Science and Technology, Ganzhou 341000, China;
2. Dongguan Eontec Co., Ltd., Dongguan 523662, China;
3. Engineering Research Center of Continuous Extrusion, Ministry of Education,
Dalian Jiaotong University, Dalian 116028, China

Abstract: The effect of the crystal orientations and precipitates on the corrosion behavior of Al−Cu−Li single crystals was studied by scanning electron microscopy, transmission electron microscopy, optical microscopy, immersion testing in exfoliation corrosion solution, and electrochemical testing. The results show that the corrosion rates of different orientations of the aged Al−Cu−Li alloy increase in the order of (001) < (101) < (111), which are different from those of the as-quenched alloy in the increasing order of (111) < (001) < (101). The precipitation of the T_1 phase deteriorated the corrosion resistance of the Al−Cu−Li alloy, and the degree of deterioration differed in different crystal plane orientations. The severe localized corrosion of the aged alloy propagates along the crystallography and extends along the $\{111\}_{Al}$ plane in the form of corrosion bands.
Key words: aluminum alloys; single crystal; corrosion; crystal orientation; precipitates

1 Introduction

Al−Cu−Li alloys are increasingly being used in the aerospace industry to achieve weight reduction. However, relevant literature [1−9] shows that Al−Cu−Li alloys are prone to local corrosion, especially the selective corrosion of some grains and grain boundaries. This corrosion also leads to the deterioration of the mechanical properties and shortening of the service life of the alloy. Therefore, it is essential to study the evolution of local corrosion over time in the new generation of highly important alloys.

The corrosion properties of Al−Cu−Li alloys depend on their compositional and microstructural characteristics [10,11]. The addition of Cu and Li to aluminum alloys leads to the precipitation of T_1 (Al₂CuLi) and δ' (Al₃Li) phases [12]. The T_1 phase is the main strengthening phase of these alloys and is closely related to the severe local corrosion of Al−Li alloys [13−20]. LI et al [21] studied the corrosion behavior of the bulk T_1 phase and believed that the T_1 phase was the anode for the alloy matrix at the early stage of corrosion and then became the cathode due to the preferential dissolution of Al and Li from the T_1 phase. MA et al [1] also showed that the origin of severe local corrosion in AA2099 alloy is related to the selective dissolution of the T_1 phase. In addition, JIANG

Corresponding author: Ji-qiang CHEN, Tel: +86-18758118522, E-mail: hermit_01@163.com;
Ying-hui ZHANG, Tel: +86-13979764105, E-mail: jxustzyh@163.com;
Ren-guo GUAN, Tel: +86-13504978164, E-mail: Guanrenguo@sina.cn

et al [22] systematically studied the corrosion behavior of Al−Cu−Li alloys aged at 160 °C for different time. It was found that the aging time directly affected the corrosion mode, from intergranular corrosion to less harmful intragrain corrosion, which was related to the precipitation of the T_1 phase at the grain boundaries and in the intragranular grains.

In addition to the significant effect of T_1 on the corrosion behavior of Al−Cu−Li alloys, the crystal orientation also plays an important role in the surface reaction, which also has a significant effect on the corrosion behavior of materials [23−27]. GUERIN et al [27] investigated the relationship between the orientation of grains in AA2050-T8 samples and the plane in which they were exposed to the electrolyte. Analysis of the samples after the corrosion tests showed that most of the corroded particles were oriented in the (111) plane relative to the exposed plane. DONATUS et al [28] observed samples of AA2198-T851 exposed to a 0.01 mol/L NaCl solution and found that after the initiation of pitting, expansion mainly occurred on the boundaries of a series of parallel cross-fringes. These fringes are related to grain orientations, and their dip angles and intersection angles vary from grain to grain.

The above reports show that the crystal orientation and precipitation of alloys have a large influence on the corrosion resistance of the alloys. However, it is difficult to accurately evaluate the influence of specific crystal orientation on the corrosion behavior of alloys when polycrystals were used as the experimental materials in previous work due to the interference of other orientations, grain boundaries and misorientations. The corrosion rate of the alloy with typical orientations (i.e., (001), (101) and (111)) cannot be accurately obtained. To solve the above problems, Al−Cu−Li single crystals with different typical orientations were prepared to study the relationship between the crystal orientation and their corrosion behavior in this study. The corrosion rates of different orientations were compared under the same corrosion conditions. In addition, the use of a single crystal can prevent precipitation at grain boundaries, and the effect of the T_1 phase on the intragranular corrosion of Al−Cu−Li alloys can be studied more specifically. Therefore, aging treatment of single crystals with different orientations was carried out to study the

influence of the corrosion behavior of single crystals with different orientations precipitated at the peak-aged state.

2 Experimental

2.1 Material pretreatment

The material used in the present work is an Al−Cu−Li alloy, and its chemical composition is Al−1.9%Cu−0.65%Li−0.15%Mg−0.15%Ag−0.01%Si−0.03%Fe (in mass fraction) determined by inductively coupled plasma atomic emission spectrometry. Al−Cu−Li single crystals were prepared by cyclic pre-strain and high-temperature annealing, which was mentioned in our previous works [29−34]. The preparation procedure is briefly described as follows: the as-quenched plates were subjected to a tensile deformation of around 1%, followed by annealing at 520 °C for 48 h. The macro-grains were produced by repeating the cycle of deformation and annealing process. The single crystals were machined from the plates.

The orientations of the single crystals were determined by electron back-scattered diffraction (EBSD), which were mounted in a ZEISS ΣIGMA scanning electron microscope (SEM). Three types of single crystals close to typical orientations (i.e., (001), (101) and (111)) were selected to study the effect of the orientations. The EBSD grain orientation maps of the selected single crystals are shown in Fig. 1. The plane orientations of the single crystals are close to (001), (101) and (111). Two groups of single crystals with three orientations were prepared to study the effect of the precipitates. Thus, one group of single crystals was kept in the as-quenched condition, and the other group was subjected to the aging treatment after water quenching.

2.2 Immersion test

The immersion test was carried out in an exfoliation corrosion (EXCO) solution (234 g NaCl + 50 g KNO_3 + 6 mL HNO_3, dilution with deionized water to 1000 mL), and the temperature was kept at (25±2) °C in a water bath. The surface morphologies of the samples were observed by optical microscopy (OM). Field-emission scanning electron microscopy (SEM, MLA650F) was used to observe the surface corrosion morphology of the single crystals with different orientations after
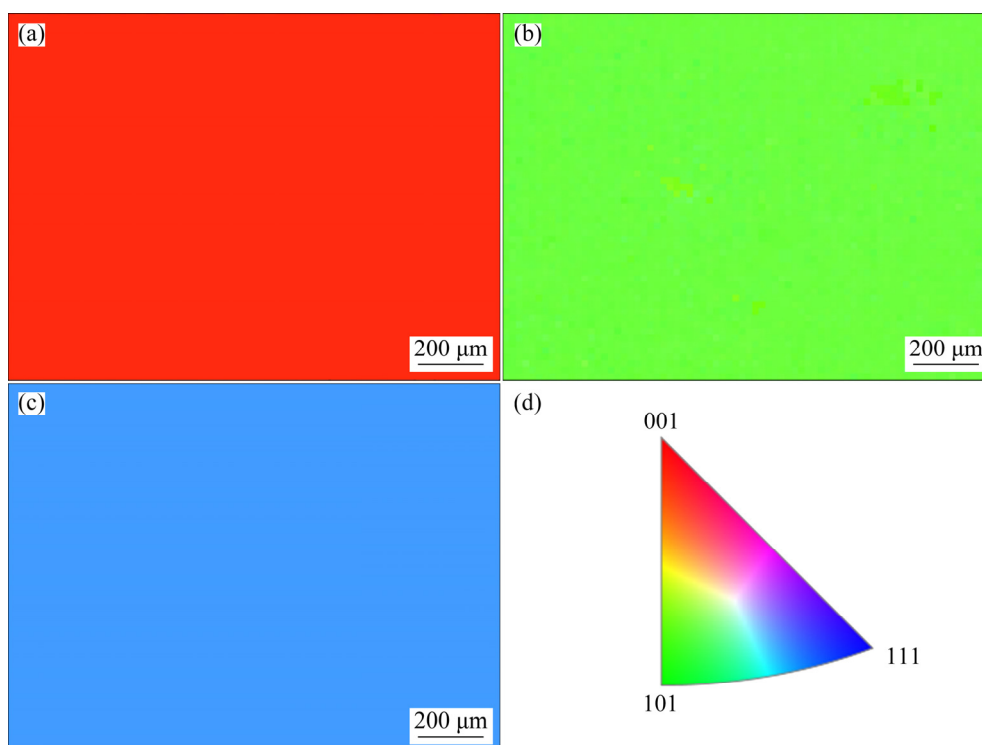
Fig. 1 EBSD orientation maps of selected single crystals with different plane orientations: (a) $(108)_{Al}$, close to (001); (b) $(6,1,10)_{Al}$, close to (101); (c) $(212)_{Al}$, close to (111); (d) Triangle-correlated each color in EBSD map with specific grain orientation

removing the corrosion products. The corrosion area of each sample was estimated by ImageJ software.

2.3 Electrochemical tests

A Princeton electrochemical workstation (PARSTAT4000A, the minimum current resolution of the electrochemical equipment used was 1.2 fA, and the minimum voltage resolution was 1.5 μV) was used to measure the potentiodynamic polarization and AC impedance. The sample was used as the working electrode (WE), platinum was used as the counter electrode (CE), and a saturated calomel electrode (SCE) was used as the reference electrode (RE). The samples were sequentially ground with serial sandpapers and then cleaned and dried. The area of the test surface was controlled to be 10 mm × 10 mm. The potentio-metric polarization was measured by scanning the potential from −0.25 to 0.25 V at a rate of 1 mV/s. Electrochemical impedance spectroscopy (EIS) tests were carried out with an alternating disturbance amplitude of 10 mV and a frequency range from 100 kHz to 0.01 Hz. The EIS data were analyzed by the "ZsimpWin" software. A solution

of 3.5 wt.% NaCl was used for the electrochemical tests, and all the results were repeated three times to ensure reproducibility in the present work.

2.4 Microstructural characterization

The precipitates were characterized by an FEI TECNAI G2 F20 S-TWIN scanning transmission electron microscope (STEM). TEM samples were mechanically thinned to 80−100 μm and then stamped into disks with a diameter of 3 mm. The specimens were prepared by twin-jet polishing in a $HNO_3 + CH_3OH$ solution at a volume ratio of 3:7. The polishing voltage and temperature range were 20 V and from −20 to −25 °C, respectively.

3 Results

3.1 Corrosion behavior of as-quenched Al−Cu−Li alloy

Figure 2 shows SEM images of morphologies of the as-quenched single crystals after immersion in the EXCO solution for 24 h. Signs of corrosion were observed on the surfaces of all single crystals, but the degree of corrosion was different in each case. After immersion for 24 h, a large amount of
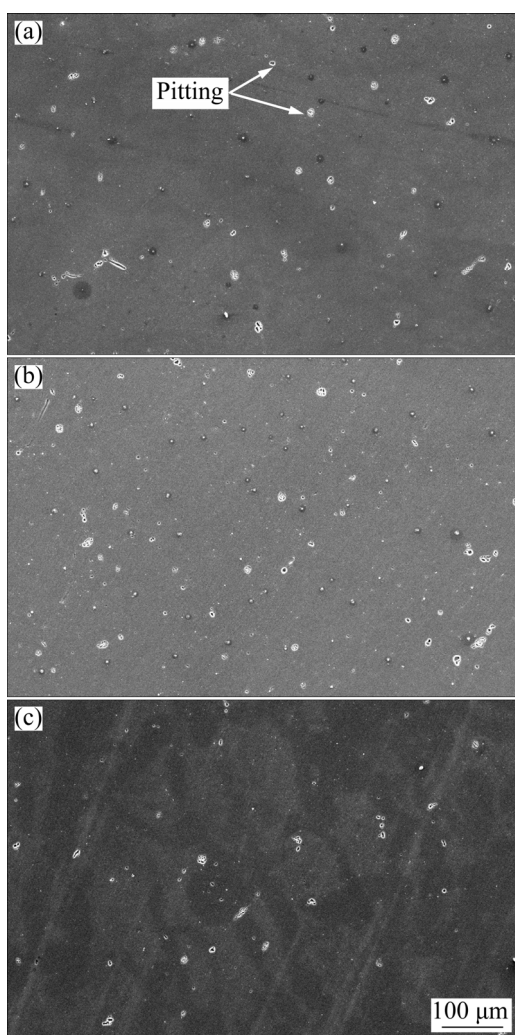
Fig. 2 SEM images of as-quenched single crystals with different orientations after immersion in EXCO solution for 24 h: (a) (001); (b) (101); (c) (111)

pitting appeared on the surface of all single crystals; however, the amount was different. The pitting amount of the single crystal with the (101) orientation was greater than that of the single crystal with the (001) and (111) orientations, and the pitting amount of the single crystal with the (111) orientation was the lowest (The corrosion area of (001)-oriented grain is approximately 1.31%, corrosion area of (101)-oriented grain is approximately 1.59%, and corrosion area of (111)-oriented grain is approximately 0.71%). These observations indicate that the corrosion rates of the as-quenched alloy with different typical orientations decrease in the order of (101) > (001) > (111) in the same corrosion environment.

In addition, pitting was observed by SEM, and the right figures display the framed area in the left

figures at increased magnification. Pitting corrosion on the surface of the alloy occurred in the form of clusters, and the pitting morphologies exhibited different geometric patterns, as shown in Fig. 3, which shows that the pitting morphology of the alloy surface is affected by the crystal orientation.

Figure 4(a) shows the variation in the open-circuit potential (φ_{OCP}) of the solution-treated alloy with different orientations in a 3.5 wt.% NaCl solution with increasing immersion time. No significant difference was found in the evolution of the φ_{OCP} among the samples with three different orientations. At the early stage, the open-circuit potential changed greatly over time but reached a stable state after 400 s of immersion. Therefore, the potentiodynamic polarization measurements in this study were conducted on the samples after sufficient soaking time (i.e., 30 min) to ensure that the φ_{OCP} reached a stable state.

To study the electrochemical corrosion behavior of the as-quenched Al−Cu−Li alloy, potentiodynamic polarization tests were conducted on the three as-quenched samples. Figure 4(b) shows the potentiodynamic polarization curves measured after immersion for 30 min at φ_{OCP}. The corrosion potential and corrosion current density of the as-quenched samples were obtained by extrapolating the Tafel curves, and the results are summarized in Table 1.

Table 1 shows that the corrosion current density decreases in the order of (101) > (001) > (111) for the as-quenched samples. A lower corrosion current density means better corrosion resistance. This suggests that the sample with the (111) orientation has the best corrosion resistance, while the sample with the (101) orientation has the worst corrosion resistance in the 3.5 wt.% NaCl solution. This result is consistent with the experimental results of Fig. 2.

3.2 Corrosion behavior of peak-aged Al−Cu−Li alloy

Figure 5(a) shows the aging hardening curve of the Al−Cu−Li alloy aged at 180 °C. The hardness reached the peak value after aging for 31 h. The precipitated phase in the peak-aged sample was characterized by TEM. Figure 5(b) shows a TEM image of the Al−Cu−Li alloy. The analysis of the selected electron diffraction (SAED) pattern shown in Fig. 5(c) confirms that the main precipitate
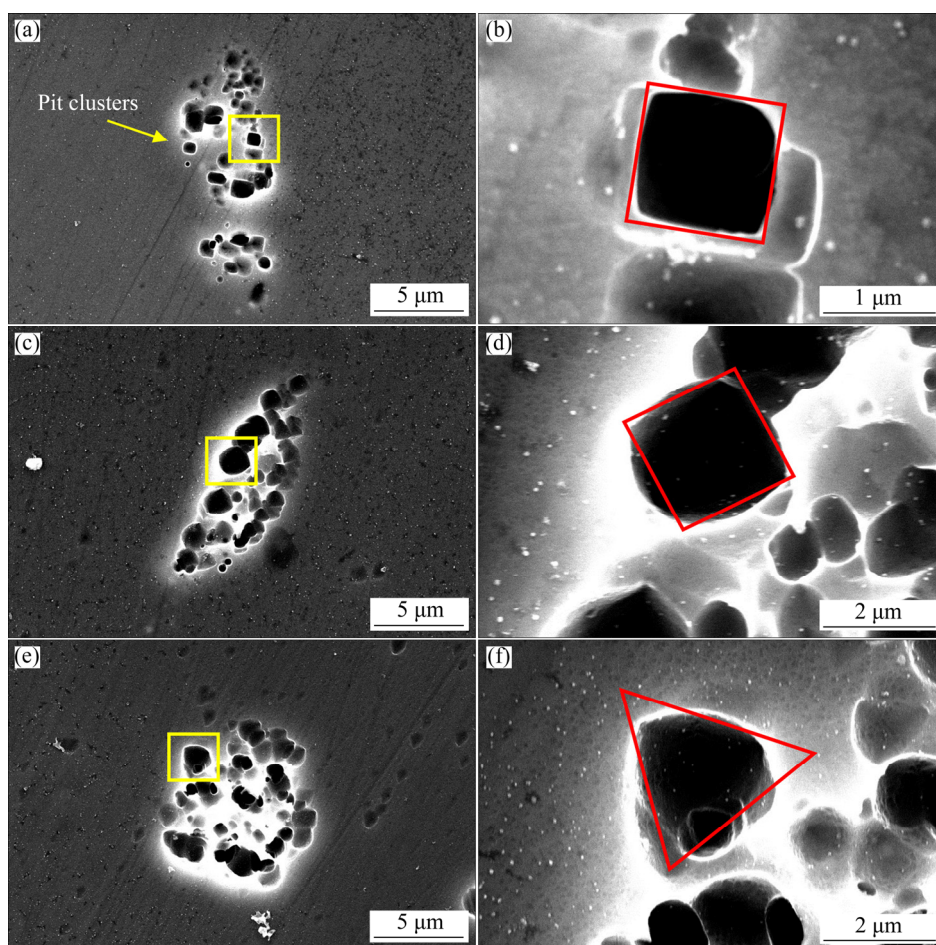
Fig. 3 Pitting morphologies of as-quenched single crystals with different orientations after immersion in EXCO solution for 24 h: (a, b) (001); (c, d) (101); (e, f) (111)
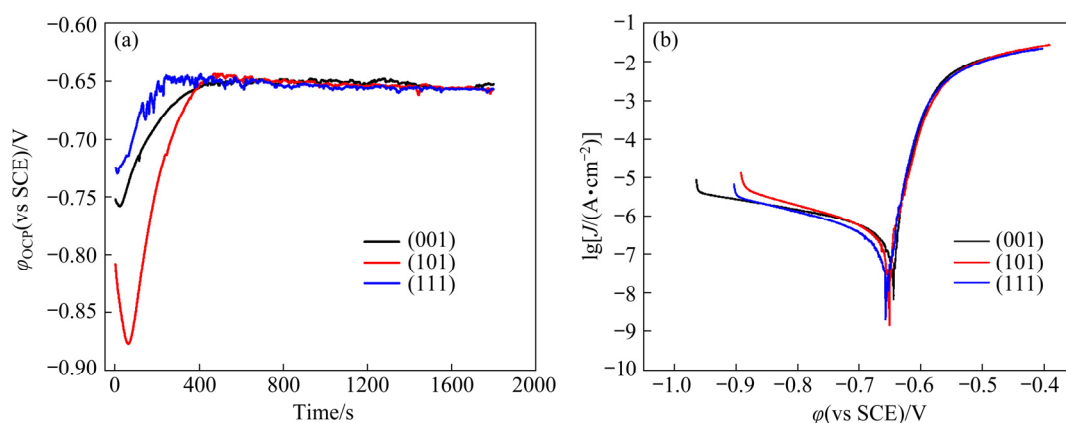

Fig. 4 Variation in open-circuit potential of as-quenched alloy in 3.5 wt.% NaCl solution (a) and potentiometric polarization curves after immersion in 3.5 wt.% NaCl solution for 30 min (b)

Table 1 Corrosion potentials and corrosion current densities of as-quenched samples with different orientations

Sample	φ_{corr}(vs SCE)/mV	J_{corr}/(nA·cm^{-2})
(001)-oriented	−644.8±5.8	132.8±9.4
(101)-oriented	−652.6±1.1	162.3±11.2
(111)-oriented	−656.0±3.9	102.4±10.6

in the Al−Cu−Li alloy is the T_1 phase. The T_1 phase has a hexagonal crystal structure and a fine needle shape (as shown in Fig. 5(d)).

An immersion test in EXCO solution was carried out with the peak-aged alloy. Figure 6 shows the morphologies of the single crystals before immersion and after immersion for 1 and
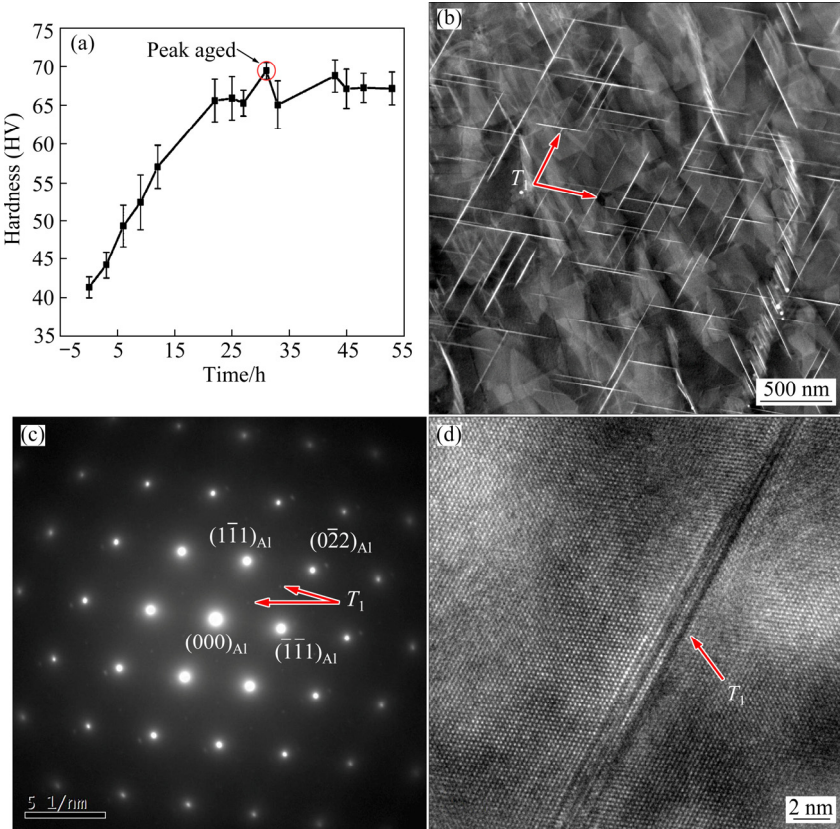
Fig. 5 Aging hardening curve of Al−Cu−Li alloy (a), TEM image of alloy under peak aging (b), selected area electron diffraction pattern of alloy (c), and high-resolution HAADF-STEM image of T_1 phase (d)
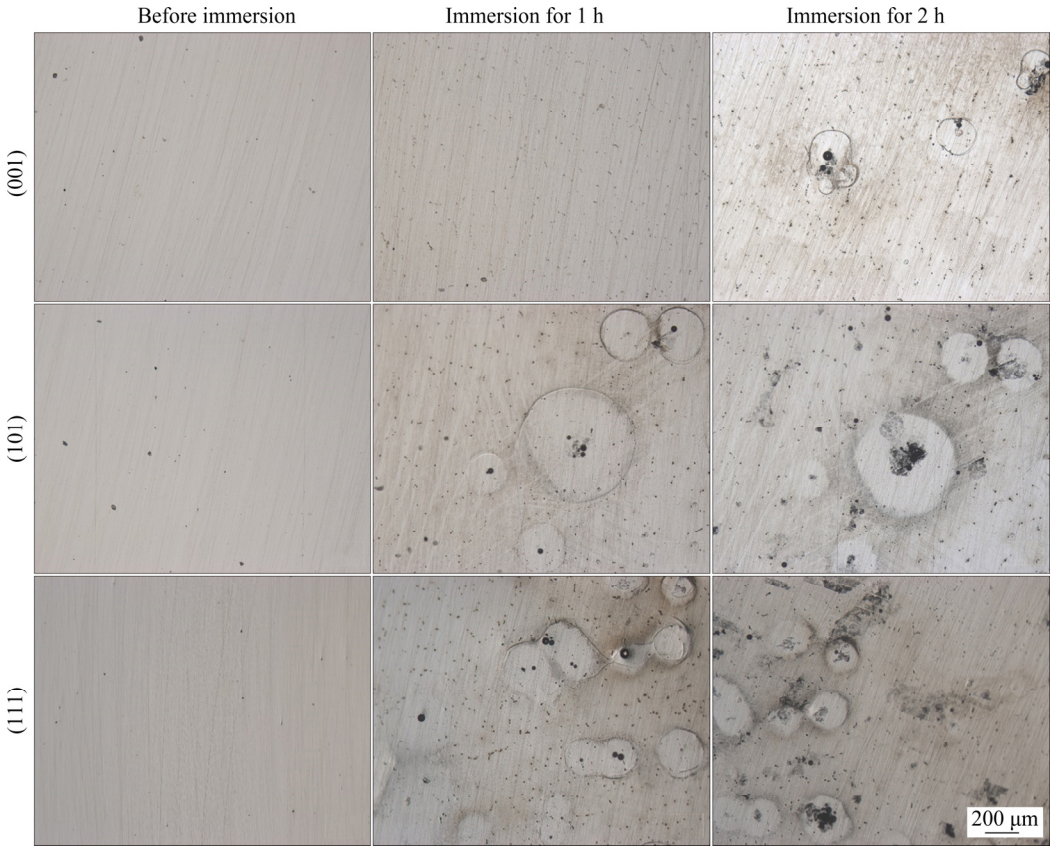

Fig. 6 OM images of aged single crystals before and after immersion in EXCO solution for 1 and 2 h

2 h. The corrosion resistances of different crystal plane orientations are slightly different. After immersion for 1 h, a large amount of pitting corrosion was observed on the surface of the single crystal with the (001) orientation, and it was evenly distributed. In addition to pitting, corrosion rings were also observed in local areas on the surface of the single crystals with the (101) and (111) orientations, and the number of corrosion rings on the surface of the single crystal with the (111) orientation was greater than that of corrosion rings on the single crystal with the (101) orientation. With increasing immersion time, corrosion rings were also found on the surface of the single crystal with the (001) orientation after 2 h of immersion, but they were still in the initial stage. For the single crystals with (101) and (111) orientations, in addition to the increase in the number of corrosion rings, severe local corrosion (SLC) pits in the center of the rings began to expand, showing crystallographic corrosion and parallel propagation in a certain direction in the form of corrosion bands.

Figure 7 shows SEM images of single crystals with the corrosion products removed after immersion for 2 h. The corrosion rings on the surface of the sample disappear. In terms of the degree of corrosion, the corrosion of the single crystal with the (111) orientation is the most serious with the largest corroded area, while the corrosion of the single crystal with the (001) orientation is the least serious with the smallest corroded area (The corrosion area of (001)-oriented grain is approximately 1.00%, corrosion area of (101)-oriented grain is approximately 2.67%, corrosion area of (111)-oriented grain is approximately 3.71%). This phenomenon can be observed not only at the microlevel but also at the macrolevel. During the immersion process, the surface of the single crystal with the (001) orientation has the fewest bubbles. In other words, the corrosion rates of the aged samples with different orientations in EXCO solution decreases in the order of (111) > (101) > (001) in the same corrosive environment.

Electrochemical tests were performed on the aged Al−Cu−Li alloy. Figure 8(a) shows the variation in the φ_{OCP} of the aged alloy with the different orientations in a 3.5 wt.% NaCl solution with increasing immersion time. The φ_{OCP} reached a stable state after a soaking time of 400 s.
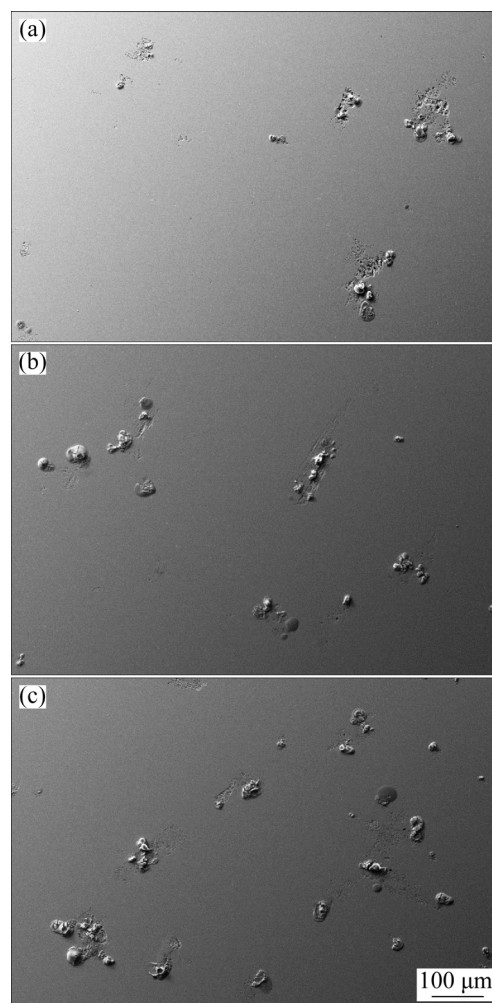

Fig. 7 SEM images of aged single crystals with corrosion products removed after immersion in EXCO solution for 2 h: (a) (001); (b) (101); (c) (111)

Figure 8(b) shows the potentiodynamic polarization curves measured after immersion for 30 min at φ_{OCP}. The results of the corrosion potential and corrosion current density of the samples with different orientations are obtained and are summarized in Table 2.

Table 2 shows that the corrosion current density decreases in the order of (111) > (101) > (001) for the aged samples, which is significantly different from the corresponding result of the as-quenched samples shown in Table 1. This indicates that the aged sample with the (001) orientation has the best corrosion resistance, while the aged sample with the (111) orientation has the worst corrosion resistance in the 3.5 wt.% NaCl solution. This result is consistent with the results of the above immersion test shown in Fig. 7.
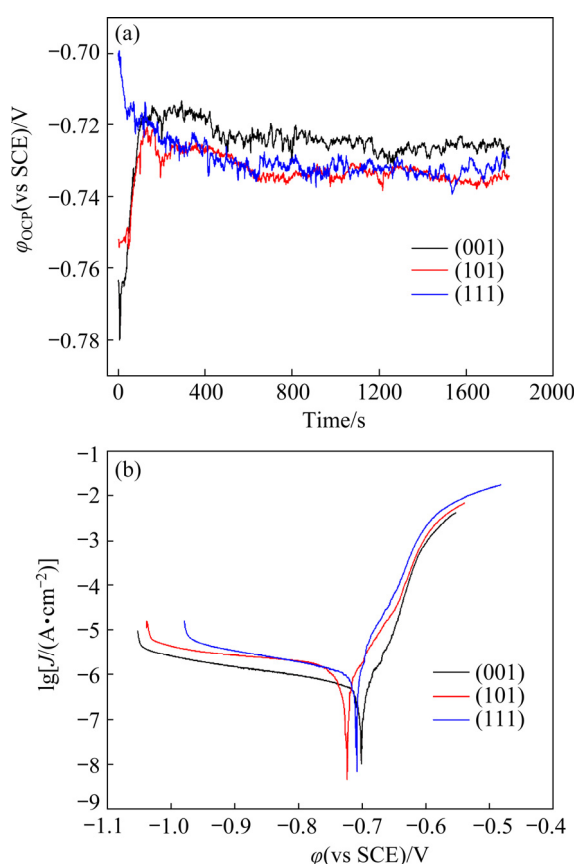
Fig. 8 Variation in open-circuit potentials of aged samples in 3.5 wt.% NaCl solution (a) and potentiometric polarization curves after immersion in 3.5 wt.% NaCl solution for 30 min (b)

Table 2 Corrosion potentials and corrosion current densities of aged samples with different orientations

Sample	φ_{corr}(vs SCE)/mV	J_{corr}/(nA·cm^{-2})
(001)-oriented	−701.0±9.0	349.1±25.3
(101)-oriented	−723.2±22.8	572.9±30.0
(111)-oriented	−710.4±6.7	650.7±34.4

To further investigate the effect of crystal orientation on the passivation film formed on the Al−Cu−Li single crystal, EIS test was performed. Figures 9(a) and (b) show the impedance spectra in the form of a Nyquist diagram, which is a capacitive reactance arc with a large radius. The arc radius of the aged samples decreases in the order of (001) > (101) > (111). Figure 9(c) shows the Bode diagram of the Al−Cu−Li alloy samples with different orientations. The diagram shows that the lg |Z| of the (001)-oriented low-frequency region is the largest and that the maximum phase angle peak of the intermediate-frequency region is wider. This
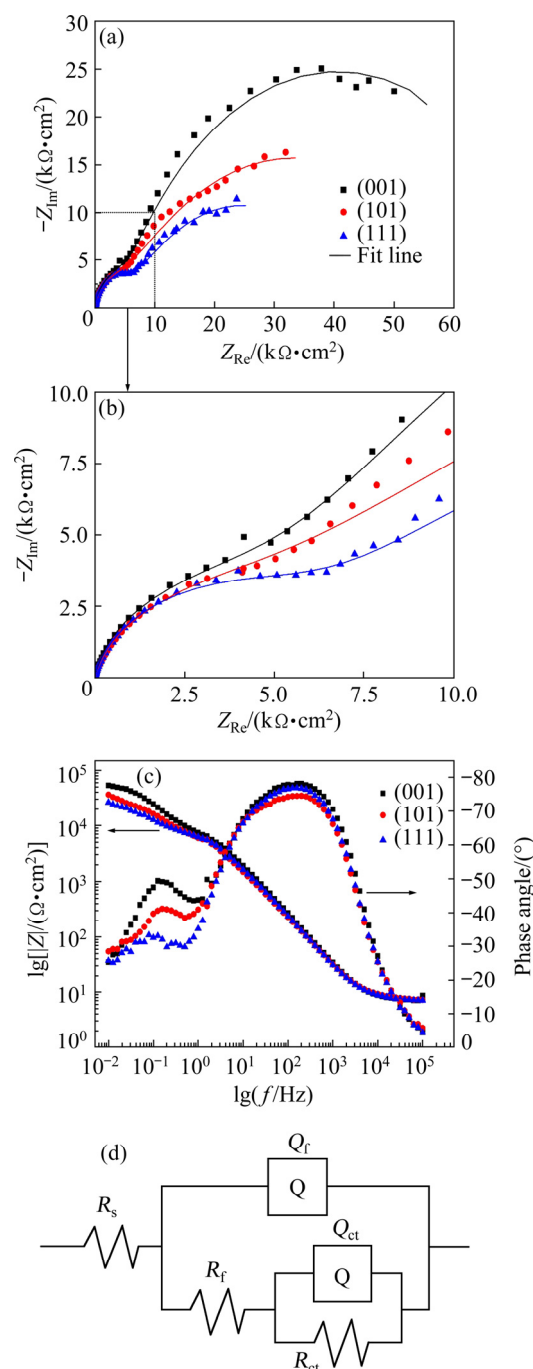

Fig. 9 EIS results of aged alloy after immersion in 3.5 wt.% NaCl solution for 30 min: (a, b) Nyquist diagrams; (c) Bode diagram; (d) Equivalent circuit

result indicated that the corrosion resistance and stability of the passivation film on the single crystal with the (001) orientation were the best.

Based on the AC impedance spectrum, the equivalent circuit shown in Fig. 9(d) was used to fit it. The fitting accuracy was on the order of 10^{-4}. It is generally considered that the equivalent circuit consists of five parts: the solution resistance (R_s); the charge transfer resistance (R_{ct}); the double-

layer capacitance (Q_{ct}); the resistance (R_f); the capacitance of the passivation film (Q_f). Q_{ct} and Q_f are the constant phase angle elements and describe the non-ideal capacitive behavior. Its impedance value can be expressed as Z_{CPE}:

$$Z_{CPE}=[Y_0(j\omega)^n]^{-1} \tag{1}$$

where Y_0 is the capacitance value, ω is the angular frequency, j is the imaginary part, and n is a physical parameter representing the interphase characteristics of the WE. When $n=1$, Q is equivalent to an ideal capacitor. When $0.8 < n < 1$, Q has a capacitive property and needs to convert Q into a true effective capacitive value C. The C value is calculated from the following effective capacitance equation [26,35]:

$$C=Q^{1/n}R^{(1-n)/n} \tag{2}$$

where R is the resistance, C_1 corresponds to the double-layer resistance R_f, and C_2 corresponds to the charge transfer R_{ct}.

The fitting parameters of the equivalent circuit components are listed in Table 3. From the fitting results, the R_f value is larger than the R_{ct} value, indicating that corrosion resistance is provided by the passivation film. For the (001)-oriented single crystal, the maximum R_f and R_{ct} values show that the passivation film has the best protection against chloride ion penetration. However, the R_f value of the (111)-oriented single crystal is the smallest, and the R_{ct} value is also the smallest, indicating that chloride ions react with metal ions more easily in the passivation film, forming destructive chlorides, accelerating the dissolution of the passivation film and reducing the corrosion resistance of the alloy. In other words, the corrosion resistance of different orientations of the Al−Cu−Li alloy decreases in the order of (001) > (101) > (111) in 3.5 wt.% NaCl solution.

4 Discussion

The results show that the corrosion behavior of the Al−Cu−Li alloy is significantly affected by the crystal orientations and precipitates. For the as-quenched samples without precipitates, the corrosion behavior also demonstrates a significant difference in different typical orientations. Generally, the corrosion behavior of the as-quenched Al alloy is mainly determined by the density of the atomic arrangement on the crystal plane. A closer atomic arrangement means better corrosion resistance. The atomic arrangement of each crystal plane is shown Fig. 10, and the order of corrosion resistance of a single-crystal orientation of Al−Cu−Li alloy is the same as the order of atomic density of the crystal plane.

In addition, the pitting shape (Fig. 3) corresponds to the atomic interstitial shape of each crystal plane. It means that the local corrosion caused by pitting of the Al−Cu−Li alloy is affected by the surface crystallography. The corrosion rates

Table 3 EIS fitting results of different orientations of Al−Cu−Li alloy in 3.5 wt.% NaCl solution

Sample	R_s/ ($\Omega \cdot cm^{-2}$)	Q_f/ ($uF \cdot cm^{-2}$)	n_1	R_f/ ($k\Omega \cdot cm^{-2}$)	C_1/ ($uF \cdot cm^{-2}$)	Q_{ct}/ ($uF \cdot cm^{-2}$)	n_2	R_{ct}/ ($k\Omega \cdot cm^{-2}$)	C_2/ ($uF \cdot cm^{-2}$)
(001)-oriented	7.283	10.84	0.9082	7.542	8.42	54.74	0.8488	69.13	69.38
(101)-oriented	7.375	13.99	0.8733	6.910	9.97	94.15	0.8132	56.16	138.02
(111)-oriented	7.197	16.14	0.8905	6.607	12.26	153.1	0.8411	37.15	212.61

n_1 and n_2 are the interphase characteristics of the WE in the double-layer reaction stage and the charge transfer reaction stage, respectively; C_1 and C_2 are the double-layer true effective capacity and the charge transfer true effective capacity, respectively.
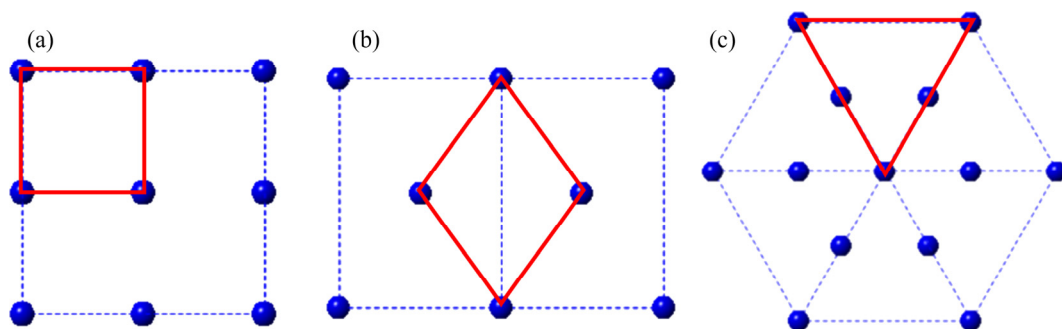

Fig. 10 Atomic arrangement of each crystal plane of Al−Cu−Li alloy: (a) (001); (b) (101); (c) (111)

of the as-quenched Al−Cu−Li single crystals with different orientations in the present work are the same as those of the as-quenched binary Al−Cu single crystals reported by our recent work [36]. The detailed explanation for the corrosion differences of the as-quenched single crystals with different typical orientations could refer to our recent work [36].

For the aged samples, an important characteristic observed from the aged samples immersed for 1 h is the evolution of corrosion. The corrosion spots surrounded by circular areas (corrosion rings) have little or no corrosion traces. The optical micrograph shown in Fig. 11(a) clearly shows the attacked and protected areas within the corrosion ring. SLC was associated with the area where hydrogen bubbles emerged during the immersion test. From Fig. 11(a), hydrogen bubbles emerge from the pit at the center of the ring, leave the alloy surface, and finally burst. This involves the following reactions [28,37]:

$$Al=Al^{3+}+3e \quad\quad\quad (3)$$

$$Al^{3+}+3H_2O^{-}=Al(OH)_3+3H^{+} \quad\quad\quad (4)$$

where H^{+} is produced by the hydrolysis of Al^{3+} to $Al(OH)_3$ according to Reaction (4). Reaction (3) gives the electrons needed for Reaction (5) to form H_2.

$$2H^{+}+2e=H_2\uparrow \quad\quad\quad (5)$$

The circular characteristics around the bubbles are attributed to the push formed by the bubbles when they burst, which pushes away the corrosion products on the alloy surface. This also explains the disappearance of the circular features when the corrosion products are removed. During the immersion test, the process of bubble generation to burst continued in the area, leading to the continuous consumption of materials in the pit and eventually leading to the formation of SLC. This characteristic can be described in Fig. 11(b). The corrosion area is regarded as a local microcell, in which the SLC pit is used as the anode to provide cathodic protection to the adjacent area to a certain extent, thus reducing the nucleation and growth rate of the surrounding pits [37].

In addition, after aging, the surface corrosion of the single crystal with the (111) orientation is the most serious. It is worth noting that the (111) plane is the surface with the highest density and the
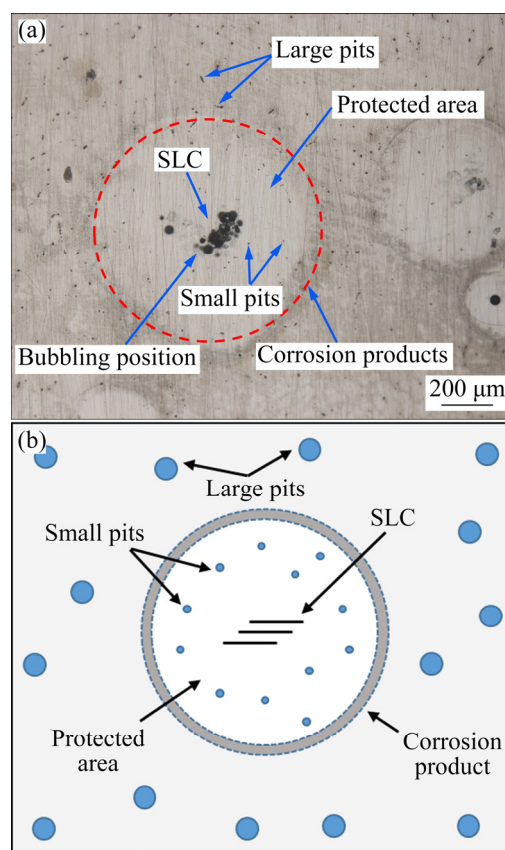
Fig. 11 OM image of alloy after immersion in EXCO solution for 2 h (a) and schematic diagram of corrosion rings (b)

habit plane of the T_1 phase. Due to the high Li content, the potential of the T_1 phase is more negative than that of the alloy matrix [10,26]. During the immersion experiment, the T_1 phase is dissolved preferentially. In the dissolution process, lithium is selectively dissolved, which increases the concentration of inactive copper. Subsequently, the copper-rich residue becomes a cathode relative to its surroundings, leading to anodic dissolution of the surrounding alloy matrix [26,38]. Regarding the (111) plane as a habit plane, the contact area of the T_1 phase on the surface is the largest, so the corrosion rate is the fastest. The (001) and (101) planes intersect only one diagonal edge with the (111) plane, but the corrosion rate of the single crystal with the (101) orientation is faster than that of the single crystal with the (001) orientation because it has the lowest atomic density. Therefore, under the same corrosion conditions, (111)-oriented grains have the worst corrosion resistance, and (001)-oriented grains have the best corrosion resistance.
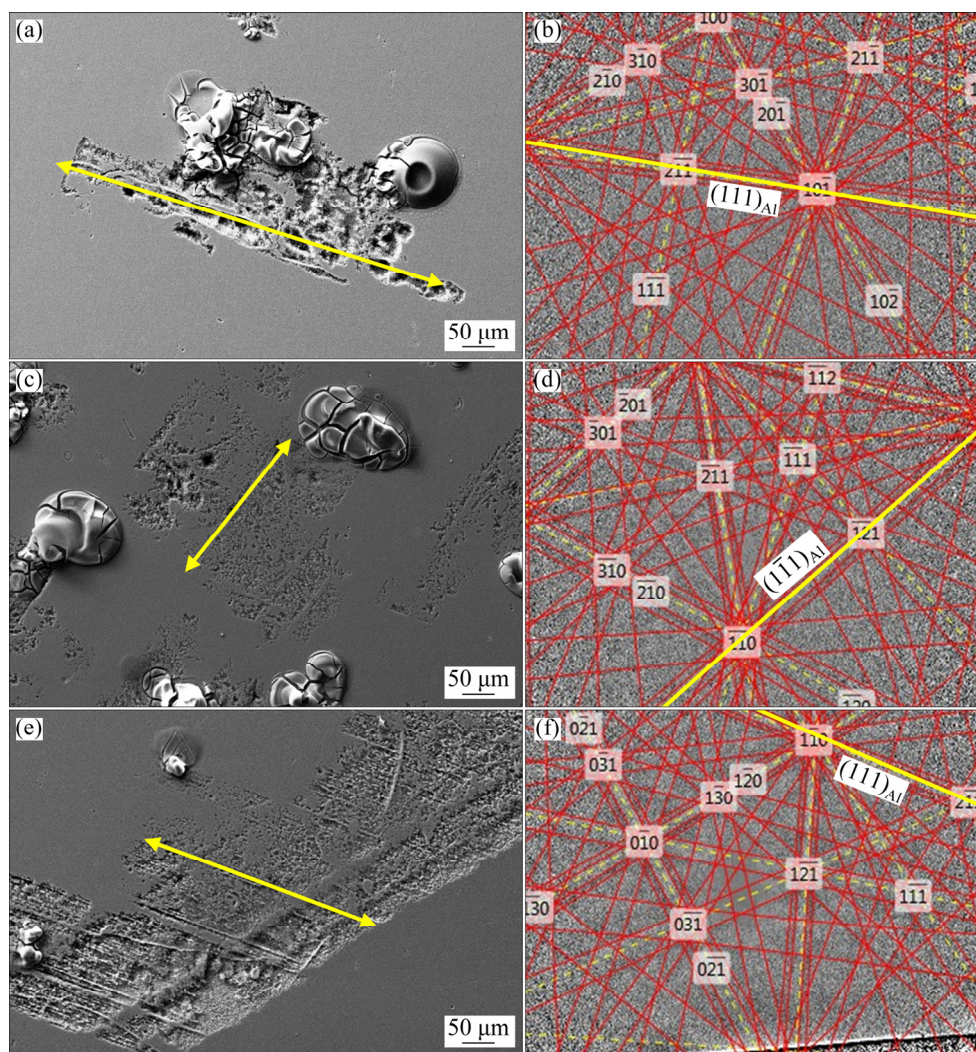
Fig. 12 SEM images of typical crystallographic corrosion (a, c, e) and Kikuchi patterns corresponding to crystal (b, d, f): (a, b) (001); (c, d) (101); (e, f) (111)

During alloy immersion, severe local corrosion propagates along crystallography, extends in the form of corrosion bands and has a certain orientation, as shown in Figs. 12(a), (c), and (e). To obtain orientation information, the corrosion bands of the three groups of samples were compared with the Kikuchi patterns of the corresponding grains (Figs. 12(b), (d), and (f)). It was found that the propagation direction of the corrosion bands was approximately parallel to the $\{111\}_{Al}$ plane, which meant that the direction of crystal corrosion in this alloy was consistent with the previous literature [25,28,39]. According to the related literature, this phenomenon is related to the precipitate phase in the alloy. However, the habit plane of the T_1 phase is just the (111) plane. This phenomenon is not found in the immersion process

of the as-quenched alloy, which also indicates that the T_1 phase is related to the local corrosion sensitivity of the Al−Cu−Li alloy.

Furthermore, compared with the as-quenched alloy immersed for 24 h, the aged alloy underwent more serious corrosion after immersion for only 2 h. Meanwhile, it can be seen that the corrosion rate of the aged alloy was higher than that of the as-quenched alloy based on the corrosion current density results (as shown in Table 1 and Table 2). This also indicated that the T_1 phase accelerated the corrosion rate of the alloy.

5 Conclusions

(1) The corrosion rates of the aged Al−Cu−Li single crystals increase in the order of (001) <

(101) < (111), which is different from that of the as-quenched samples in the increasing order of (111) < (001) < (101).

(2) The precipitation of the T_1 phase deteriorated the corrosion resistance of the Al−Cu−Li alloy. The effect of the T_1 phase on the corrosion behavior of the aged single crystals with different orientations is associated with the contact area between the T_1 phase and the crystal plane.

(3) The corrosion of the aged alloy mainly extends in the form of corrosion bands that are parallel to the $\{111\}_{Al}$ plane. This is associated with the preferential dissolution of the T_1 phase during the immersion test due to the high electrochemical activity of the T_1 phase.

(4) Electrochemical analysis results indicate that the passivation film is the most stable for the aged single crystal with the (001) orientation. In contrast, the passivation film is the most unstable for the aged single crystal with (111) orientation, and it has the worst corrosion resistance.

Acknowledgments

References

[1]   MA Y, ZHOU X, HUANG W, TOMPSON G E, ZHANG X, LUO C, SUN Z. Localised corrosion in AA2099-T83 aluminium−lithium alloy: The role of grain orientation [J]. Corrosion Science, 2016, 107: 41−48.

[2]   ZHU Ya-kun, POPLAWSKY J D, LI Si-rui, UNOCIC R R, BLAND L G, TAYLOR C D, LOCKE J S, MARQUIS E A, FRANKEL G S. Localized corrosion at nm-scale hardening precipitates in Al−Cu−Li alloys [J]. Acta Materialia, 2020, 189: 204−213.

[3]   LIU Dan-yang, SANG Feng-jian, LI Jin-feng, BIRBILIS N, WANG Zhi-xiu, MA Yun-long, ZHANG Rui-feng. The role of grain structure characteristics on the localised corrosion feature in the 1445 Al−Cu−Li alloy [J]. Materials Characterization, 2019, 158: 109981.

[4]   QIN Ying, WU Guo-hua, ATRENS A, ZHANG Xiao-long, ZHANG Liang, DING Wen-jiang. Effect of NaOH concentration on microstructure and corrosion resistance of MAO coating on cast Al−Li alloy [J]. Transactions of Nonferrous Metals Society of China, 2021, 31: 913−924.

[5]   ZHANG X, ZHOU X, HASHIMOTO T, LINDSAY J, CIUCA O, LUO C, SUN Z, ZHANG X, TANG Z. The influence of grain structure on the corrosion behaviour of 2A97-T3 Al−Cu−Li alloy [J]. Corrosion Science, 2017, 116: 14−21.

[6]   LIU Dan-yang, MA Yun-long, LI Jin-feng, ZHANG Rui-feng, IWAOKA H, HIROSAWA S. Precipitate microstructures, mechanical properties and corrosion resistance of Al−1.0wt.%Cu−2.5wt.%Li alloys with different micro-alloyed elements addition [J]. Materials Characterization, 2020, 167: 110528.

[7]   CHEN Xiao-xue, MA Xin-wu, ZHAO Guo-qun, WANG Yiong-xiao, XU Xiao. Effects of re-solution and re-aging treatment on mechanical property, corrosion resistance and electrochemical behavior of 2196 Al−Cu−Li alloy [J]. Materials & Design, 2021, 204: 109662.

[8]   LUO Chen, ALBU S P, ZHOU Xiao-rong, SUN Zhi-hua, ZHANG Xiao-yun, TANG Zhi-hui, THOMPSON G E. Continuous and discontinuous localized corrosion of a 2xxx aluminium−copper−lithium alloy in sodium chloride solution [J]. Journal of Alloys and Compounds, 2016, 658: 61−70.

[9]   PROTON V, ALEXIS J, ANDRIEU E, DELFOSSE J, BLANC C. The influence of artificial ageing on the corrosion behaviour of a 2050 aluminium−copper−lithium alloy [J]. Corrosion Science, 2014, 80: 494−502.

[10]   ARAUJO J V D S, DONATUS U, QUEIROZ F M, TERADA M, MILAGRE M X, ALENCAR M C D, COSTA I. On the severe localized corrosion susceptibility of the AA2198-T851 alloy [J]. Corrosion Science, 2018, 133: 132−140.

[11]   XU Wei-feng, MA Jun, WANG Miao, LU Hong-jian, LUO Yu-xuan. Effect of cooling conditions on corrosion resistance of friction stir welded 2219-T62 aluminum alloy thick plate joint [J]. Transactions of Nonferrous Metals Society of China, 2020, 30: 1491−1499.

[12]   LI Jin-feng, HUANG Jia-lei, LIU Dan-yang, CHEN Yong-lai, ZHANG Xu-hu, MA Peng-cheng. Distribution and evolution of aging precipitates in Al−Cu−Li alloy with high Li concentration [J]. Transactions of Nonferrous Metals Society of China, 2019, 29: 15−24.

[13]   WEN Feng, CHEN Ji-qiang, HAN Shuang, YE Jie-yun, REN Jie-ke, ZHANG Ying-hui, LI Wei-rong, GUAN Ren-guo. The initial corrosion behavior of Al−Cu−Li bicrystals: Effect of misorientation and precipitates [J]. Journal of Materials Research and Technology, 2022, 18: 3716−3724.

[14]   MENG Qiang, LIU Yang, KANG Ju, FU Rui-dong, GUO Xiao-yan, LI Yi-jun. Effect of precipitate evolution on corrosion behavior of friction stir welded joints of AA2060-T8 alloy [J]. Transactions of Nonferrous Metals Society of China, 2019, 29: 701−709.

[15]   HUANG Jia-lei, LI Jin-feng, LIU Dan-yang, ZHANG Rui-feng, CHEN Yong-lai, ZHANG Xu-hu, MA Peng-cheng,

GUPTA R K, BIRBILIS N. Correlation of intergranular corrosion behaviour with microstructure in Al−Cu−Li alloy [J]. Corrosion Science, 2018, 139: 215−226.

[16] WANG Shao-gang, HUANG Yan, ZHAO Li. Effect of aging treatment on corrosion resistance of Al−Li alloy joint welded by electron beam welding [J]. Rare Metal Materials and Engineering, 2018, 47: 1973−1979.

[17] HUANG Wei-jiu, MA Yan-long, ZHOU X, MENG X, LIAO Y, CHAI L, YI Y, ZHANG X. Correlation between localized plastic deformation and localized corrosion in AA2099 aluminum-lithium alloy [J]. Surface and Interface Analysis, 2015, 48: 838−842.

[18] MA Y L, ZHOU X, HUANG W J, LIAO Y, CHEN X, ZHANG X, THOMPSON G E. Crystallographic defects induced localized corrosion in AA2099-T8 aluminium alloy [J]. Corrosion Engineering, Science and Technology, 2015, 50: 420−424.

[19] YAN Y, PEGUGT L, GHARBI O, DESCHAMPS A, HUTVHINSON C R, KAIY S K, BIRBILIS N. On the corrosion, electrochemistry and microstructure of Al−Cu−Li alloy AA2050 as a function of ageing [J]. Materialia, 2018, 1: 25−36.

[20] ZHANG Jia-yi, WANG Bin, YI Dan-qing. Stress corrosion cracking behavior in 2297 Al−Cu−Li alloy at different grain orientations [J]. Materials Science and Engineering, 2019, 764: 138252.

[21] LI J F, ZHENG Z Q, LI S C. Simulation study on function mechanism of some precipitates in localized corrosion of Al alloys [J]. Corrosion Science, 2007, 49: 2436−2449.

[22] JIANG Bo, WANG Hai-sheng, TIAN Yu, YI Dan-qing, LIU Hui-qun, HU Zhan. Effects of aging time on corrosion behavior of an Al−Cu−Li alloy [J]. Corrosion Science, 2020, 173:108759.

[23] ZAKARIA S A, ANASYIDA A S, ZUHAILAWATI H, DHINDAW B K, JABIT N A, ISMAIL A. Characterization of mechanical and corrosion properties of cryorolled Al 1100 alloy: Effect of annealing and solution treatment [J]. Transactions of Nonferrous Metals Society of China, 2021, 31: 2949−2961.

[24] HUANG Jia-ying, FENG Si-yu, LI Shi-yong, WU Cui-lan, CHEN Jiang-hua. The crystallographic corrosion and its microstructure in an Al−Cu−Li alloy [J]. Journal of Alloys and Compounds, 2021, 861: 158588.

[25] ZHANG Xin-xin, ZHOU Xiao-rong, LIU Bing, LUO Chen. Corrosion behaviour of 2A97-T6 Al−Cu−Li alloy: The influence of non-uniform precipitation [J]. Corrosion Science the Journal on Environmental Degradation of Materials & Its Control, 2018, 132: 1−8.

[26] YANG Yan-qiu, WEN Zhi-xun, ZHAO Yan-chao, WANG Jia-po, YUE Zhu-feng. Effect of crystallographic orientation on the corrosion resistance of Ni-based single crystal superalloys [J]. Corrosion Science, 2020, 170: 108643.

[27] GUERIN M, ALEXIS J, ANDRIEU E, LAFFONT L, LEFEBVRE W, ODEMER G, BLANC C. Identification of the metallurgical parameters explaining the corrosion susceptibility in a 2050 aluminium alloy [J]. Corrosion Science, 2016, 102: 291−300.

[28] DONATUS U, TERADA M, OSPINA C R, QUEIROZ F M, COSTA I. On the AA2198-T851 alloy microstructure and its correlation with localized corrosion behaviour [J]. Corrosion Science, 2018, 131: 300−309.

[29] CHEN Ji-qiang, DENG Yun-lai, GUO, Xiao-bin. Revisit the stress-orienting effect of θ' in Al−Cu single crystal during stress aging [J]. Materials Characterization, 2018, 135: 270−277.

[30] CHEN Ji-qiang, CHEN Zhi-guo, DENG Yun-lai, GUO Xiao-bin, REN Jie-ke. Effect of loading orientations on the microstructure and property of AlCu single crystal during stress aging [J]. Materials Characterization, 2016, 117: 35−40.

[31] CHEN Ji-qiang, CHEN Zhi-guo, GUO Xiao-bin, REN Jie-ke, DENG Yun-lai. Microstructure and property of stress aged Al−Cu single crystal under various applied stresses [J]. Transactions of Nonferrous Metals Society of China, 2016, 26: 2838−2845.

[32] CHEN Ji-qiang, LIU Chao, LI Qi-long, YAO Mao-hai, ZHOU Qiong-yu, ZHAO Hong-jin. Stress aging of Al−Cu−Mg−Ag single crystal: The effect of the loading orientations [J]. Journal of Alloys and Compounds, 2020, 816: 152635.

[33] CHEN Ji-qiang, LIU Chao, LI Qi-long, ZHAO Hong-jin. A three-dimensional characterization method for the preferentially oriented precipitation of Ω-phase in stress-aged Al−Cu−Mg−Ag single crystal [J]. Materials Characterization, 2019, 153: 184−189.

[34] CHEN Ji-qiang, CHEN Zhi-guo, GUO Xiao-bin, DENG Yun-lai. Changing distribution and geometry of S' in Al−Cu−Mg single crystals during stress aging by controlling the loading orientation [J]. Materials Science and Engineering A, 2016, 650: 154−160.

[35] HIRSCHORN B, ORAZEM M E, TRIBOLLET B, VIVIER V, FRATEUR I. Determination of effective capacitance and film thickness from constant-phase-element parameters [J]. Electrochimica Acta, 2010, 55: 6218−6227.

[36] WEN Feng, CHEN Ji-qiang, ZHONG Shi-biao, ZHOU Zi-xiang, HAN Shuang, WEI Hai-gen, ZHANG Ying-hui. Effect of crystal orientations and precipitates on the corrosion behavior of the Al−Cu alloy using single crystals [J]. Journal of Alloys and Compounds, 2022, 890: 161858.

[37] LEI X, SAATCHI A, GHANBARI E, DANG R, LI W, WANG N, MACDONALD D D. Studies on pitting corrosion of Al−Cu−Li alloys part I: Effect of Li addition by microstructural, electrochemical, in-situ, and pit depth analysis [J]. Materials, 2019, 12: 1600.

[38] ZHAO Kuo, LIU Jian-hua, YU Mei, LI Song-mei. Through-thickness inhomogeneity of precipitate distribution and pitting corrosion behavior of Al−Li alloy thick plate [J]. Transactions of Nonferrous Metals Society of China, 2019, 29: 1793−1802.

[39] ARAUJO J, BUGARIN A, DONATUS U, MACHADO C, COSTA I. Thermomechanical treatment and corrosion resistance correlation in the AA2198 Al−Cu−Li alloy [J]. Corrosion Engineering Science and Technology, 2019, 54: 575−586.

晶体取向及析出相对 Al–Cu–Li 单晶腐蚀行为的影响

文 锋 [1]，陈继强 [1,2]，韩 双 [1]，周子翔 [1]，钟世标 [1]，张迎晖 [1]，李卫荣 [2]，管仁国 [1,3]

1. 江西理工大学 材料冶金化学学部，赣州 341000；

2. 东莞宜安科技股份有限公司，东莞 523662；

3. 大连交通大学 连续挤压教育部工程研究中心，大连 116028

摘　要：通过扫描电子显微镜、透射电子显微镜、光学显微镜、剥落腐蚀溶液浸泡实验和电化学测试研究晶体取向和析出相对 Al–Cu–Li 单晶腐蚀行为的影响。结果表明，时效态 Al–Cu–Li 合金不同取向的腐蚀速率按(001) < (101) < (111)的顺序增加，与淬火态合金的腐蚀速率按(111) < (001) < (101)的顺序增加明显不同。T_1 相的析出恶化了 Al–Cu–Li 合金的耐蚀性，且不同晶面取向的恶化程度不同。时效态合金的严重局部腐蚀沿着晶体学方向扩展，并以腐蚀带的形式沿{111}$_{Al}$ 面扩展。

关键词：铝合金；单晶；腐蚀；晶体取向；析出相

(Edited by Wei-ping CHEN)